Document downloaded from:

http://hdl.handle.net/10251/183156

This paper must be cited as:

Szalad, H.; Peng, L.; Primo Arnau, AM.; Albero-Sancho, J.; García Gómez, H. (2021). Fe clusters embedded on N-doped graphene as a photothermal catalyst for selective CO2 hydrogenation. Chemical Communications. 57(78):10075-10078. https://doi.org/10.1039/d1cc03524j

The final publication is available at

https://doi.org/10.1039/d1cc03524j

Copyright The Royal Society of Chemistry

Additional Information

COMMUNICATION

Fe clusters embedded on N-doped graphene as photothermal catalyst for selective CO_2 hydrogenation

Received 00th January 20xx,
Accepted 00th January 20xx

DOI: 10.1039/x0xx00000x

Horatiu Szalad,[a] Lu Peng,[a] Ana Primo,[a] Josep Albero *[a] and Hermenegildo García*[a]

In comparison with Co analog, small Fe clusters incorporated in graphene matrix exhibit a photo-assisted increase of 110 % in the reverse water gas shift CO_2 hydrogenation under UV-Vis light irradiation. Available data indicates that the photo-assistance derives from light absorption by the N-doped graphene followed by charge recombination at the Fe clusters, increasing their local temperature.

CO_2 conversion into fuels and chemicals is currently attracting much interest due to the increasing concern about atmospheric emissions of this greenhouse gas and its consequence on the global warming and climate change.[1] Among the different approaches explored so far, the photo-assisted CO_2 conversion into fuels and chemicals is very appealing, since it can be based on the use of inexhaustible and environmental-friendly solar energy.[2] In addition, photo-assisted CO_2 conversion is performed under milder temperature and pressure than analogous catalytic processes.[2]

Photo-assisted CO_2 conversion can be carried out through two general mechanisms. In the so-called photothermal mechanism, a *nanoheater* acting as active site converts the energy of photons into local heat at the nanometre scale and the high temperature allows to overcome kinetic barriers at the catalytic centre.[2, 3] In contrast to the photothermal pathway, other alternative mechanism denoted as photocatalytic CO_2 conversion is based on photoinduced generation of electron/hole pairs, followed by subsequent multiple coupled electron and proton transfer reactions to form the target products.[4] The photocatalytic mechanism requires photons of energy larger than the bandgap and it suffers from the competition of electron/hole recombination, resulting in general in low conversion efficiencies. On the other hand, in the photothermal process, large metal nanoparticles having plasmon band in the visible region extending into the NIR can be efficient to promote local heating, but due to the required large size for plasmon absorption they are catalytically less active than they could be if the particle size were smaller. One of the main advantages of the photothermal process vs. the conventional thermocatalytic reaction is that it can be performed in a range of apparent macroscopic temperatures in which the traditional catalytic process does not occur or reaches only low CO_2 conversions. That is, energy utilization in the photothermal pathway is more efficient, since heat is produced at the metal nanoparticle where the reaction occurs, reaching higher CO_2 conversion than analogous thermocatalytic process based on the heating of the whole system. However, it would be desirable to develop a photothermal CO_2 conversion using small metal clusters that do not even exhibit a plasmon band due to their small size, but they can exhibit high catalytic activity.

Metal or metal oxide-containing materials have been widely employed in photothermal CO_2 conversion.[3, 5] Among them, those containing noble metals (Au, Pt, Pd, etc.) or containing critical raw materials, such as Ru, In, etc. have demonstrated high photo-assisted CO_2 conversions and production rates. However, for the sake of sustainability, the use of abundant, non-critical, first-row transition metals supported on suitable substrates is more convenient. Thus, for instance, Fe and Ni based photothermal catalysts, obtained from layered double hydroxides, have recently demonstrated CO_2 conversion efficiencies of 52.9 and 78.4%, respectively.[6, 7] Alternatively, graphene (G) and derivatives, especially those obtained from the pyrolysis of biomass wastes, have recently attracted much attention as support of metal or metal oxides in photo-assisted CO_2 reduction.[8, 9] Among the properties that justify the interest of G as support, the most relevant ones are its large surface area, strong substrate adsorption, possibility to provide charge density, the rational design of active sites and the strong interaction between transition metals and G due to the overlapping between the d and π orbitals in metals and g, respectively. Thus, Cu_2O nanoparticles supported on defective G has demonstrated to be an efficient photocatalyst for CO_2 hydrogenation obtaining a maximum specific CH_4 formation rate of approximately 15 mmol /g·h at 250 ^oC and 200 mW/cm^2 irradiation.[10] Similarly, NiO/Ni nanoparticles supported on defective G have been tested as photocatalysts for CO_2

[a] *Instituto Universitario Mixto de Tecnología Química (CSIC-UPV), Universitat Politécnica de Valéncia (UPV), Avda. de los Naranjos s/n, 46022, Valencia (Spain).*
Electronic Supplementary Information (ESI) available: Synthetic procedures, ADF-STEM and HRFESEM images, Raman spectra, CO evolution using (N)C, Mass spectrum, CO evolution at different temperatures, CO evolution at different light intensity, diffuse reflectance UV-Vis, XPS and TPD analysis. See DOI: 10.1039/x0xx00000x

Please do not adjust margins

hydrogenation, reaching a CH_4 production rate of 642 µmol/g·h at 200 °C under 223.6 mW/cm^2.[11] Alternatively, NiO nanoparticles supported on graphitic carbon nitride demonstrated photothermal CO_2 conversion to CH_4 at a rate of 28 µmol/g·h under 150 °C and 108 mW/cm^2 light irradiation conditions.[12] In all these examples, photo-assisted CO_2 conversion is carried out under near atmospheric pressure and temperatures for which the thermocatalytic process does not occur or is negligible. In comparison to CH_4 evolution, photo-assisted CO_2 conversion to CO via the reverse water gas shift (RWGS) reaction using first-row transition metal or metal oxides supported on G or related materials has been less investigated.

This manuscript reports the contrasting thermocatalytic vs. photothermal activity of two materials composed by N-doped graphitic carbon matrix ((N)C) containing minute amounts of Fe (Fe@(N)C) or Co (Co@(N)C) for the selective RWGS CO_2 conversion to CO. The novelty of our study is that the photothermal process occurs on small (subnanometric) Fe clusters that do not exhibit observable plasmon band. Evidence on the reaction mechanism indicates that the photothermal effect derives from the recombination of the photogenerated charge carriers generated on the N-doped G at the Fe clusters, rather than direct light harvesting by these small metal clusters.

The samples of the present study are small Fe or Co clusters embedded in a graphitic carbon matrix. Fe@(N)C and Co@(N)C were prepared from acid aqueous solutions of chitosan (as (N)C precursor) containing adsorbed $Fe(OAc)_2$ or $Co(OAc)_2$ (as precursors of the metal clusters), respectively. The solutions were added dropwise to aqueous NaOH that causes the instantaneous precipitation of chitosan hydrogel microspheres. After water exchange by EtOH, Fe^{2+} or Co^{2+} were chemically reduced by $NaBH_4$ in EtOH prior to supercritical CO_2 drying and pyrolysis under Ar at 900 °C (see Supplementary Information for details of the synthetic procedure).

The concentration of the $Fe(OAc)_2$ and $Co(OAc)_2$ precursors in the impregnation step were adjusted in order to obtain final Fe and Co loadings about 0.05 wt.% in Fe@(N)C and Co@(N)C samples. High angular Dark-Field (HADF) Scanning Transmission Electron Microscopy (STEM) and High-Resolution Field Emission Scanning Electron Microscopy (HRFESEM) images (see Fig. S1 in Supplementary Information) of Fe@(N)C and Co@(N)C samples show in both cases a loose coral-like morphology of the graphitic carbon matrix, with no evidence of metal particles. Elemental mapping of representative Fe@(N)C and Co@(N)C STEM images confirms the presence of Fe and Co elements, respectively, homogeneously distributed on the (N)C matrix (see Fig.S2 in Supplementary Information).

Raman spectra of (N)C, Fe@(N)C and Co@(N)C samples revealed the typical 2D (2700 cm^{-1}), G (1580 cm^{-1}) and D (1350 cm^{-1}) bands characteristic of defective G obtained from the pyrolysis of chitosan (Fig. S3 in Supplementary Information). However, no obvious vibration bands for Fe or Co oxides or carbides were observed. X-Ray Diffraction (XRD) patterns (not shown) of Fe@(N)C and Co@(N)C samples present a broad and low intensity peak at 26.5°, attributed to π-π layer stacking in graphitic carbon matrix. However, no evidence of Fe or Co crystalline phases was detected, in accordance with the low metal loading and high metal dispersion in these samples.

X-ray Photoelectron Spectroscopy (XPS) measurements were performed in order to evaluate the oxidation state of the Fe species in Fe@(N)C (Fig. S4 in Supplementary Information). The high-resolution C1s peak shows the typical components of N-doped defective G obtained from chitosan pyrolysis. The main component was attributed to sp^2 carbon (284.5 eV), while components related to C-O and C-N bonds were also detected in good agreement with the O 1s spectrum. The N 1s peak revealed the presence of quaternary and pyridinic N typical of N-doped G, as well as a minor component attributed to N-oxide, as reported before.[13] The Fe 2p spectrum shows a small signal centred at 710.68 eV, attributed to Fe^{3+} species.

The oxidation state of the Fe species in Fe@(N)C was further investigated by Temperature-Programmed Reduction (TPR) using H_2 as reducing agent (Fig. S5 in Supplementary Information). The TPR experimental profile of Fe@(N)C presented a not well-resolved reduction peak between 250 and 650 °C, with maximum at 416 °C. This is not only attributed to the Fe^{3+} to Fe^{+2} reduction, but also to the Fe^{2+} to Fe^0. The observation of this broad peak instead of well-resolved H_2 uptake for each reduction process could be attributed to the low Fe loading in the samples. Quantification of H_2 consumption from the TPR measurement resulted in a 0.051 wt.% Fe, in good agreement with the ICP-OES analysis. In view of the TPR data, it is worth noticing that the studied reaction temperature (245 °C) could not be enough to fully reduce the Fe^{+3} species in Fe@(N)C to Fe^{2+} or Fe^0.

Photothermal CO_2 hydrogenation reactions were carried out in a cylindrical quartz reactor equipped with an electrical heating ribbon that allows to heat the reactor at the required temperature. Fe@(N)C and Co@(N)C samples were placed as a thin bed under the illuminated reactor area and the photoreactor was loaded with 1-to-1 partial pressures of H_2 and CO_2 to a total pressure of 1.4 bar. The photoreactor temperature was equilibrated in the dark prior irradiation with UV-Vis light from a 300 W Xe-lamp, which emission spectrum comprises from 330 to 800 nm, approximately.

The activity of Fe@(N)C and Co@(N)C samples was tested for the photoassisted RWGS reaction, obtaining in both cases CO as the only detectable product in the temperature range under study. The obtained CO evolution using Fe@(N)C and Co@(N)C under different conditions are summarized in Table S1 in Supplementary Information. Control experiments testing the activity of (N)C under identical conditions showed that the total CO amount obtained after 24 h is at least one order of magnitude lower than that obtained with Fe@(N)C sample (Fig. S6 in Suppl. Inf.), indicating that the metal sites are responsible for the catalytic activity of Co@(N)C and Fe@(N)C.

As can be observed in Fig. 1 and Fig. S7 in Suppl. Inf., the CO production after 24 h reaction using Fe@(N)C and Co@(N)C, respectively, at 245 °C and 120 mW/cm^2 irradiation was of 319 and 1805 µmol of CO/$g_{catalyst}$, respectively. Fe@(N)C and Co@(N)C samples were also catalytically active at 245 °C in the dark (Fig. 1, Fig. S7 and Table S1), but with lesser CO formation. It is worth noticing that despite Co@(N)C is more active than

Please do not adjust margins

Fe@(N)C, both in light and dark, the CO evolution using Co@(N)C sample was not significantly enhanced by light (~30 %) (Fig. S7). On the contrary, a ~110% enhancement in CO evolution was observed under light when Fe@(N)C sample was used (Fig. 1). These results indicate that while Co has demonstrated to be an efficient thermochemical catalyst for this reaction, its ability to promote light-assisted catalysts is very limited.

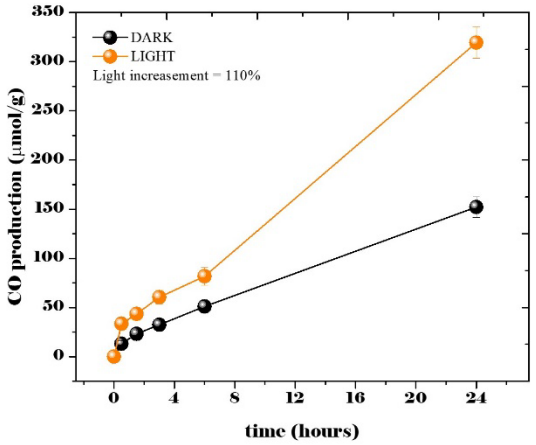

Figure 1. CO evolution using Fe@(N)C photocatalysts at 245 °C under 120 mW/cm^2 illumination (orange) and dark conditions (black). Reaction conditions: 40 mg of photocatalyst, partial pressures for H_2 and CO_2 0.7 bar, UV–vis light from a Xe lamp at 1200 W/m^2 irradiation. Lines between the experimental points just indicate the trend.

In contrast, Fe@(N)C, which has demonstrated lower thermocatalytic activity, presents much larger photo-response. Control experiments using isotopically labelled $^{13}CO_2$, monitoring ^{13}CO formation along time by mass spectrometry (MS), were carried out (Fig. S8 in Suppl. Inf.). The MS spectra recorded for the formed ^{13}CO conclusively confirmed $^{13}CO_2$ gas as the main source of ^{13}CO, and it grows with time.

To gain further insights into the reaction mechanism of the photo-assisted RWGS promoted by Fe@(N)C, CO_2 reduction reaction was tested at different temperatures between 205 and 288 °C under light (120 mW/cm^2) and dark conditions. The results are presented in Fig. S9 in Suppl. Inf. As presented there, the CO production rate increased exponentially with the temperature, following the Arrhenius equation (inset Fig. S9 (b)), both in light and dark conditions. The experimental apparent activation energy (E_a) values upon light irradiation and dark conditions are 83 and 75 kJ/mol, respectively. These E_a values are similar both in light and dark conditions, suggesting that the reaction follows in both cases, photoassisted and thermochemical, a similar mechanism with the same rate determining step. The difference would be that heat is provided locally at the metal cluster in the photothermal reaction, while the thermochemical process requires the heating of the whole system.

The influence of the light intensity on the CO production was also investigated (Fig. S10 in Supplementary Information). CO evolution at 245 °C upon different light intensities showed a bi-modal behaviour. Between dark and 60 mW/cm^2 irradiation power, the CO evolution increased linearly a 28 %. However, from 60 to 120 mW/cm^2 the CO production grows faster, over 85%, corresponding to 3-fold faster in this light power range. This indicates that a high photon flux is required to significantly enhance the photothermal activity in this material.

The Fe@(N)C spectral response was also studied. As can be seen in Fig. S11 in Supplementary Information, the CO evolution at 245 °C in the dark and upon irradiation with the output of the 300 W Xe lamp filtered with a 360 nm cut-off filter were coincident. This is indicating that only high energy UV photons are contributing to the photoassisted CO evolution by Fe@(N)C. Diffuse reflectance spectra of (N)C and Fe@(N)C shows coincident absorption spectra (See Fig. S12 in supplementary Information). In both cases, a prominent band in the UV region due to N-doping of G can be observed. Tauc plot obtained from the diffuse reflectance UV-Vis spectra (inset Fig. S12) revealed that Fe@(N)C presents a slightly larger bandgap (3.17 eV) than that of the (N)G support (3.10 eV). The obtained Fe@(N)C band gap confirms that photo-assistance of RWGS in Fe@(N)C only occurs upon UV irradiation, meaning that light is absorbed by (N)G. It is reported that upon light absorption (N)G undergoes charge separation in e^- and h^+.[13]

Finally, Fe@(N)C stability for CO evolution was tested performing a series of consecutive reuses of the same sample. In these recycling experiments, Fe@(N)C was tested for 6 h periods at the hardest reaction conditions (288 °C and 120 mW/cm^2 irradiation). During each cycle, the evolved CO was measured. Each new cycle started with exhaustive system purging to completely remove the produced CO in the previous run, prior to CO_2 and H_2 loading, subsequent 288 °C heating and 6 h irradiation test. This procedure was repeated 3 additional times. The temporal gas evolution in the four consecutive cycles is presented as Fig. S13 in Supplementary Information. As it can be seen there, Fe@(N)C shows nearly constant CO production for the four consecutive runs, demonstrating its robustness for this reaction under these reaction conditions.

In order to gain information on the photo-assisted RWGS mechanism, photocurrent measurements were carried out for (N)C, Co@(N)C and Fe@(N)C samples. Fig. 2 shows that Fe@(N)C exhibits a 2.7-fold photocurrent enhancement compared to (N)C. Notably, Co@(N)C showed very similar photocurrent than (N)C, indicating that at low loadings Co species in Co@(N)C are not photoactive, in good agreement with the results of the photo-assisted RWGS reaction. On the contrary, Fe@(N)C sample has demonstrated to be photocatalytically active, enhancing significantly the CO production with the aid of light and photocurrent measurements shows that this sample undergoes charge separation upon irradiation.

To gain further information of the effect of light, Transient Absorption (TA) measurements were performed for (N)G, Fe@(N)C and Co@(N)C upon 355 nm laser excitation. The results are presented in Fig. S14 in Supplementary Information. As can be seen there, the TA spectra of the different samples present a continuous absorption decreasing in intensity towards the NIR, as reported before.[13] However, the Fe@(N)C TA spectrum shows lower signal intensity than the Co@(N) and (N)C. Since the signal intensity have been normalized by the optical absorption density at the excitation wavelength (355

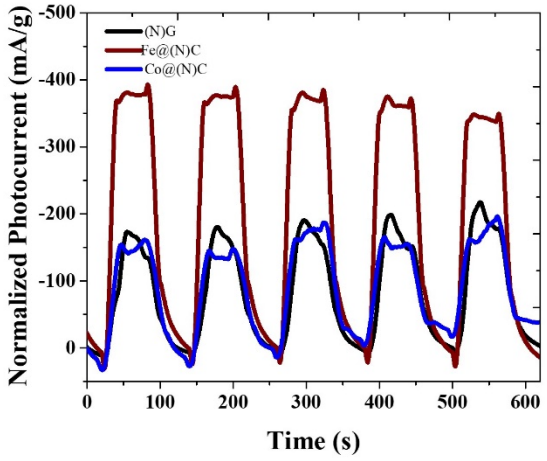

Figure 2. Photocurrent measurements of electrodes prepared by depositing (N)C, Fe@(N)C and Co@(N)C on FTO electrode (1.5 × 1 cm^2). Electrolyte: 0.1 M $LiClO_4$ in acetonitrile. Five consecutive cycles of 60 s were carried out switching on and off UV–vis light from a Xe lamp at 1200 W/m^2 irradiation while photocurrent values were acquired.

nm), the lesser intensity in the Fe@(N)C spectrum can be ascribed to the decrease in the transient species concentration. The nature of these transient species has been investigated by means of quenching experiments (Fig. S15 in Supplementary Information). As can be seen, MeOH addition (15 %vol.) produced an almost complete quenching of the Fe@(N)C excited states, while in saturated CO_2 atmosphere the TA signal did not suffered significant changes. These results indicate that the detected transient species corresponds, mainly, to holes.

Moreover, the TA kinetics were measured at 500 and 660 nm. For both wavelengths, signal decay exhibits a bi-modal kinetics, exhibiting fast (< 300 ns) and slow (in the μs time scale) components. From fitting of the experimental data to Eq. 1, lifetimes of 119.7 and 123.7 ns for the fast component of (N)C and Co(N)C, respectively, were determined, while the fast component lifetime of Fe@(N) was much shorter, 48.6 ns. Similarly, the slow component lifetimes were 16.7, 12.4 and 9.7 μs for (N)C, Co@(N)C and Fe@(N)C, respectively. Overall, the decreased signal intensity, together with the faster excited state kinetics points out to more efficient and faster charge recombination kinetics in Fe(N)C than Co@C(N) and (N)C. It is proposed that upon UV absorption by defective (N)G and generation of e^- and h^+, Fe clusters are acting as efficient recombination centres where photogenerated charges are annihilated through non-radiative mechanism. The recombination energy will promote heating at the Fe clusters. Thus, an apparent photothermal mechanism by the local temperature increase at Fe clusters occurs, even if this is triggered by a prior photocatalytic charge separation process. This combination of the two pathways (first photocatalytic at (N)G, then photothermal at Fe clusters) has been already reported by Ozin et al. in a Ru/SiO_2 based photocatalyst.

$$F(t) = K \cdot a_1 \cdot e^{-\tau 1 t} + a_2 \cdot e^{-\tau 2 t} \qquad \text{Eq. 1}$$

In conclusion, while Co@(N)C is an efficient thermochemical catalyst, photoassistance for the RWGS in Co@(N) is minor compared to analogous Fe@(N)C that has a 110 % CO production increase upon UV light irradiation. Insights into the mechanism of the light assistance indicates that (N)C is the light harvesting component, exhibiting photocurrent compatible with the occurrence of charge separation. Lifetime measurements and quenching studies by TA indicates that Fe clusters are acting as e^-/h^+ recombination centres. Compatible with the similar activation energy, it is proposed that the after harge recombination at the Fe clusters, a photothermal effect increasing the local temperature at the Fe clusters is responsible for the observed positive effect of light. Accordingly, the photo-assisted response of Fe@(N)C is a unique case of photoinduced charge separation followed by a photothermal effect at metal clusters of small size.

Author Contributions

L.P. prepared and characterized the catalysts. H.S. performed the photocatalytic reactions and mechanistic experiments. A.P. supervised the materials preparation and characterization. J. A. performed the TA measurements. The work was supervised by J.A. and H.G. who wrote the draft. The manuscript was revised by all the authors.

There are no conflicts to declare.

Notes and references

1. G. P. Peters, R. M. Andrew, T. Boden, J. G. Canadell, P. Ciais, C. Le Quéré, G. Marland, M. R. Raupach and C. Wilson, *Nature Climate Change*, 2013, **3**, 4-6.
2. Z. Yang, Y. Qi, F. Wang, Z. Han, Y. Jiang, H. Han, J. Liu, X. Zhang and W.-J. Ong, *Journal of Materials Chemistry A*, 2020.
3. E. T. Kho, T. H. Tan, E. Lovell, R. J. Wong, J. Scott and R. Amal, *Green Energy & Environment*, 2017, **2**, 204-217.
4. I. I. Alkhatib, C. Garlisi, M. Pagliaro, K. Al-Ali and G. Palmisano, *Catalysis Today*, 2020, **340**, 209-224.
5. H. Liu, L. Shi, Q. Zhang, P. Qi, Y.-h. Zhao, Q. Meng, X. Feng, H. Wang and J. Ye, *Chemical Communications*, 2021.
6. Z. Li, J. Liu, R. Shi, G. I. N. Waterhouse, X.-D. Wen and T. Zhang, 2021, **11**, 2002783.
7. Z. Li, R. Shi, J. Zhao and T. Zhang, *Nano Research*, 2021, DOI: 10.1007/s12274-021-3436-6.
8. S. Remiro-Buenamañana and H. García, *ChemCatChem*, 2019, **11**, 342-356.
9. J. Albero, Y. Peng and H. García, *ACS Catalysis*, 2020, **10**, 5734-5749.
10. D. Mateo, J. Albero and H. García, *Energy & Environmental Science*, 2017, **10**, 2392-2400.
11. D. Mateo, J. Albero and H. Garcia, *Applied Catalysis B: Environmental*, 2018, **224**, 563-571.
12. J. Barrio, D. Mateo, J. Albero, H. García and M. Shalom, *Advanced Energy Materials*, 2019, **9**, 1902738.
13. H. G. Baldoví, M. Álvaro, B. Ferrer and H. García, *ChemPhysChem*, 2016, **17**, 958-962.